JGR Space Physics

RESEARCH ARTICLE
10.1029/2019JA026757

Characteristics of Relativistic Microburst Intensity From SAMPEX Observations

E. Douma[1], C. J. Rodger[1], L. W. Blum[2], T. P. O'Brien[3], M. A. Clilverd[4], and J. B. Blake[3]

[1]Department of Physics, University of Otago, Otago, New Zealand, [2]NASA Goddard Space Flight Center, Greenbelt, MD, USA, [3]The Aerospace Corporation, El Segundo, CA, USA, [4]British Antarctic Survey (NERC), Cambridge, UK

Key Points:
- There is little variation in the average relativistic microburst flux magnitudes with changing geomagnetic activity
- Number of relativistic microbursts appears to be controlled by variations in trapped flux magnitudes and geomagnetic activity
- Intensity of relativistic microbursts appears to have no correspondence to trapped flux magnitudes

Correspondence to:
E. Douma,
emmadouma@gmail.com

Citation:
Douma, E., Rodger, C. J., Blum, L. W., O'Brien, T. P., Clilverd, M. A., & Blake, J. B. (2019). Characteristics of relativistic microburst intensity from SAMPEX observations. *Journal of Geophysical Research: Space Physics*, *124*. https://doi.org/10.1029/2019JA026757

Received 24 MAR 2019
Accepted 6 JUL 2019
Accepted article online 18 JUL 2019

Abstract Relativistic electron microbursts are an important electron loss process from the radiation belts into the atmosphere. These precipitation events have been shown to significantly impact the radiation belt fluxes and atmospheric chemistry. In this study we address a lack of knowledge about the relativistic microburst intensity using measurements of 21,746 microbursts from the Solar Anomalous Magnetospheric Particle Explorer (SAMPEX). We find that the relativistic microburst intensity increases as we move inward in L, with a higher proportion of low-intensity microbursts (<2,250 [MeV cm^2 sr s]$^{-1}$) in the 03–11 magnetic local time region. The mean microburst intensity increases by a factor of 1.7 as the geomagnetic activity level increases and the proportion of high-intensity relativistic microbursts (>2,250 [MeV cm^2 sr s]$^{-1}$) in the 03–11 magnetic local time region increases as geomagnetic activity increases, consistent with changes in the whistler mode chorus wave activity. Comparisons between relativistic microburst properties and trapped fluxes suggest that the microburst intensities are not limited by the trapped flux present alongside the scattering processes. However, microburst activity appears to correspond to the changing trapped flux; more microbursts occur when the trapped fluxes are enhancing, suggesting that microbursts are linked to processes causing the increased trapped fluxes. Finally, modeling of the impact of a published microburst spectra on a flux tube shows that microbursts are capable of depleting <500-keV electrons within 1 hr and depleting higher-energy electrons in 1–23 hr.

1. Introduction

It is widely accepted that the net electron flux in the radiation belts is "a delicate balance between electron acceleration and loss processes" (Reeves et al., 2003). An important electron loss process from the radiation belts into the atmosphere that has recently gained new attention are relativistic electron microbursts. These intense precipitation events of >1-MeV electrons on timescales of <1 s have been widely studied (e.g., Blum et al., 2015; Lorentzen et al., 2001; Nakamura et al., 1995; O'Brien et al., 2003) and estimates of their affect on the radiation belt environment have been conducted. Lorentzen et al. (2001) estimated that relativistic microbursts occurring during a single storm of 6-hr duration could empty the entire relativistic electron population from the radiation belts. They used two different values for the relativistic microburst intensity based on individual case studies; 275 (cm^2 sr s)$^{-1}$ and ~2,000 (cm^2 sr s)$^{-1}$. Breneman et al. (2017) estimated that microbursts could deplete an entire flux tube of 220-keV electrons within ~10 hr and could deplete the higher energies on even shorter timescales. Recently, Greeley et al. (2019) found that microburst activity is a significant contributor to the global electron decay observed in the recovery phase of coronal mass ejection-driven geomagnetic storms.

There has also been an attempt at quantifying the atmospheric impact of relativistic microbursts. Seppälä et al. (2018) used a statistically average microburst occurrence rate (three microbursts per minute) and intensity (~1,300 [cm^2 sr s]$^{-1}$) over a 6-hr storm and modeled the impact on HO_x, NO_x, and ozone. They found that these statistically average microburst events caused a significant 10–20% loss of ozone in the upper stratosphere and lower mesosphere. This ozone loss was due to the production of both HO_x and NO_x (Seppälä et al., 2018).

Based on these relatively new studies, Breneman et al. (2017), Greeley et al. (2019), and Seppälä et al. (2018), we now know that relativistic microbursts are not only a significant loss process from the electron radiation belts but also a significant driver of chemical changes and subsequently ozone loss in the atmosphere.

With the launch of the microburst CubeSat, FIREBIRD II (Focused Investigations of Relativistic Electron Burst Intensity, Range, and Dynamics), there has been a renewed interest in relativistic microbursts and new developments in the field. Most notably, there have been some case study estimates of the relativistic microburst spatial scale sizes (Anderson et al., 2017; Crew et al., 2016; Shumko et al., 2018) as well as a one to one correspondence between microburst activity and whistler mode chorus wave activity (Breneman et al., 2017). The spatial sizes of microbursts appear to be consistent with the spatial extent of a single chorus element (e.g., Agapitov et al., 2017, Agapitov et al., 2018). In conjunction with other recent studies (Douma et al., 2017; Douma et al., 2018) it has been suggested that relativistic microbursts are predominantly driven by whistler mode chorus waves. For example, in Douma et al. (2017) a large statistical study of Solar Anomalous Magnetospheric Particle Explorer (SAMPEX) observed relativistic electron microbursts was conducted, producing the same statistical data set used in the current study. The authors contrasted the magnetic local time (MLT) and L occurrence distributions of the microbursts, particularly the geomagnetically dependent microburst occurrence distributions with those for whistler mode chorus and electromagnetic ion cyclotron (EMIC) waves. In a later study by Douma et al. (2018) a series of case studies were undertaken, investigating the occurrence of whistler mode chorus and EMIC waves in ground-based data when SAMPEX-reported microbursts occurred nearby. Both these studies concluded that chorus was likely the dominant driver for microbursts but could not rule out that some events might be EMIC driven. Whistler mode chorus waves are typically described as discrete structures of wave elements with timescales of 100 ms and sweep rates of 8 kHz/s (Santolik et al., 2008). Chorus wave elements lie in the frequency range from a few hundreds of hertz to several kilohertz (see reviews by; Omura et al., 1991; Sazhin & Hayakawa, 1992, and references therein). However, it is important to note that the Omura and Zhao (2013) proposed EMIC scattering process should provide an additional mechanism capable of causing relativistic microbursts. Evidence for the occurrence of this scattering mechanism was reported by Douma et al. (2018). They presented case study evidence of EMIC waves occurring concurrently with relativistic microbursts, while there was no observed whistler mode chorus wave activity occurring.

A significant property of relativistic microbursts that has not been well studied to date is the intensity of the individual microbursts, that is, the quantity of electron flux that is being precipitated during these events. The authors are only aware of two such studies: Blum et al. (2015) and Greeley et al. (2019). Blum et al. (2015) found that relativistic microbursts occurring during high-speed stream-driven storms had no significant magnitude variation over different storm phases and rather remained approximately constant at 10^3 $(\mathrm{MeV\,cm^2\,sr\,s})^{-1}$. However, they did show a magnitude variation in the L range, $L = 3$–8 (Blum et al., 2015). In contrast, Greeley et al. (2019) found average microburst intensities were higher in the afternoon MLT region when compared to the morning MLT region.

In our study we address this lack of knowledge concerning relativistic microburst intensity. We use the SAMPEX Heavy Ion Large Telescope (HILT) instrument and apply the O'Brien et al. (2003) detection algorithm to identify relativistic microbursts. We also use the Blum et al. (2015) extension to the detection algorithm to describe the relativistic microburst intensity, producing a large database of events. We then investigate the distribution of the relativistic microburst intensities over L and MLT and consider how these change with changing geomagnetic activity levels. We also compare the relativistic microburst intensity and occurrence to the level of trapped flux measured by HEO3 at the time of the microburst scattering process and consider how this may affect the relativistic microburst properties. Finally, we estimate the impact of the relativistic microburst activity on the electron population in a given flux tube.

2. Instrumentation

In this study we use the HILT instrument onboard the SAMPEX to study microbursts. SAMPEX observations have been widely used previously in relativistic microburst investigations (e.g., Nakamura et al., 1995; Lorentzen et al., 2001; Greeley et al., 2019), and the O'Brien et al. (2003) detection algorithm (discussed in the following section) was specifically developed for use with SAMPEX measurements, where there is a long time series of measurements available. The HILT instrument is capable of measuring >1.05-MeV electrons and >5-MeV protons (Klecker et al., 1993). We use Row 4 of the solid state detector array (SSD4), which has a temporal resolution of 100 ms over the lifetime of the satellite. Detailed descriptions of the HILT instrument and SAMPEX satellite are given in Klecker et al. (1993) and Baker et al. (1993) and summarized in Douma et al. (2017).

There are three caveats that should be accounted for when using SAMPEX data. (1) The HILT instrument samples different pitch angles over different regions of the Earth (Dietrich et al., 2010). This caveat will be addressed in the following section. (2) The HILT instrument responds to both electrons and protons. Thus, to use the SAMPEX electron data, we must remove the proton contamination. This contamination occurs during solar proton events and in the region of the South Atlantic Magnetic Anomaly, where inner belt protons can reach SAMPEX altitudes. (3) The SAMPEX HILT instrument saturates at ~7,000 (MeV cm^2 sr s)$^{-1}$. However, only 0.15% of the SAMPEX HILT SSD4 fluxes exceed the saturation level. We thus conclude that the saturation of the SAMPEX HILT instrument will not impact our relativistic microburst intensity analysis.

In this study we also use spacecraft 1997-068 (also known as HEO3), which was launched in 1997 into a highly elliptical orbit with an inclination of −62° (Blake et al., 1997; O'Brien et al., 2007; Ripoll et al., 2015). The HEO3 satellite crosses the magnetic equator at $L \sim 2$, meaning the majority of the outer zone particle data is taken far from the equator (O'Brien et al., 2007). The HEO3 orbits begin at perigee and are divided into inbound, outbound, even, odd, high altitude, and low altitude. The satellite has variable temporal resolution over its lifetime; however, the most common temporal resolution is 15 s. HEO3 carries dosimeters and an electron-proton telescope that are capable of measuring >0.13-, >0.23-, >0.45-, >0.63-, >1.5-, and >3.0-MeV electrons and >0.080-, >0.160-, >0.320-, >5-, 8.5–35-, 16- to 40-, and 27- to 45-MeV protons (O'Brien et al., 2007; Ripoll et al., 2015). The electron data have been corrected for contamination by trapped and solar protons (O'Brien et al., 2007).

3. Event Selection

We have used the O'Brien et al. (2003) relativistic microburst detection algorithm to identify relativistic microbursts in the SAMPEX data. This algorithm has been discussed in detail in both O'Brien et al. (2003) and Douma et al. (2017). It detects sharp spikes in the precipitating fluxes by comparing the 100-ms flux data changes to 3-s smoothed baseline values. Any flux data changes 10 times greater than the baseline values are defined as microbursts. Blum et al. (2015) undertook sensitivity tests on the O'Brien et al. (2003) algorithm and found that the 10 times threshold picked up most microbursts while minimizing false detections. Examples of detected microbursts from this algorithm have been published in Blum et al. (2015, Figure 2a), Douma et al. (2017, Figure 1), and Douma et al. (2018, Figures 2–4).

In order to quantify the precipitating electron flux magnitude (hereafter referred to as intensity) of the relativistic microbursts, we have used the Blum et al. (2015) extension to the O'Brien et al. (2003) detection algorithm. The Blum et al. (2015) extension is as follows:

$$M = N_{100} - B_{3000}, \tag{1}$$

where M is the magnitude of the microbursts (in counts), N_{100} is the number of counts in 100 ms (i.e., a single data point), and B_{3000} is the baseline counts, defined as the 10th percentile in 3,000 ms (3 s) bins.

The removal of the baseline value in the calculation of the relativistic microburst intensity is thought to account for the contribution of the trapped and drift loss cone electrons. However, upon closer inspection of the microburst intensities it is clear that the drift loss cone fluxes still lead to contamination in the intensity calculation. As such, we have limited our analysis of the relativistic microburst intensities to the North Atlantic Region where the SAMPEX HILT instrument is only measuring the bounce loss cone fluxes (Dietrich et al., 2010).

We have defined the North Atlantic Region from 30–65°N in latitude and 278–36°E in longitude. The yellow shaded region in Figure 1 identifies this North Atlantic Region. The upper latitude limit increases with increasing eastward longitude in the range 278–305°E. Beyond 305°E the upper latitude limit remains constant at 65°N. This definition of the North Atlantic Region follows the region outlined in Figure 3 of Dietrich et al. (2010) where SAMPEX is only sampling the bounce loss cone. In the North Atlantic Region we detect 21,746 relativistic microbursts in the SAMPEX HILT data from 23 August 1996 to 11 August 2007. Beyond 2007 SAMPEX was in spin mode, during which results from the detection and magnitude algorithm are no longer reliable.

4. Flux Magnitude Characteristics

We show the distribution of the relativistic microburst >1.05-MeV intensities in Figure 2. From these distributions it is clear that the majority of relativistic microbursts identified have intensities between 100

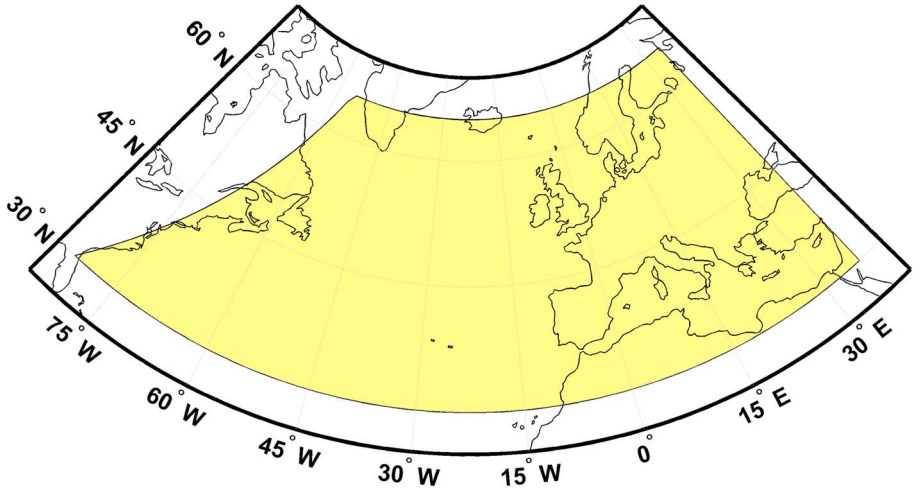

Figure 1. The yellow shaded region identifies the North Atlantic Region used in our study. This is the region where Solar Anomalous Particle Explorer samples the bounce loss cone, and the detection and magnitude algorithm is reliable.

and 1,000 (MeV cm^2 sr s)$^{-1}$. The number of microbursts with intensities higher than 1,000 (MeV cm^2 sr s)$^{-1}$ falls off roughly exponentially. There are no relativistic microbursts detected with intensities below 30 (MeV cm^2 sr s)$^{-1}$. This lower limit on the relativistic microburst intensities is possibly due to the detection algorithm, which requires the flux "spike" to exceed a certain threshold in order to be identified as a relativistic microburst. The high-intensity cutoff in the relativistic microburst intensities observed on the $\log_{10}$ scale (Figure 2b) is likely due to the SAMPEX HILT instrument saturation. However, the very small number of microburst events leading up to this high-intensity cutoff suggests that the missing high-intensity relativistic microbursts are unlikely to affect the statistics presented in this paper.

4.1. *L* and MLT Distributions

In Figure 3 we present the McIlwain *L* and MLT distributions of the relativistic microburst intensity. We have calculated the mean and associated 95% confidence interval for *L* and MLT values where ≥5 relativistic microbursts are occurring to ensure our results are statistically representative of the relativistic microburst intensity data set.

From Figure 3a we observe that the mean microburst intensity peaks at $L = 4.5$ with 1,554 (MeV cm^2 sr s)$^{-1}$. The peak intensity is a factor of ~3 larger than the mean intensities at $L = 3$ and $L = 8$.

Figure 3b shows that there is less variation in microburst intensities over MLT than is observed over *L*. There is a statistically significant minimum in the relativistic microburst intensity at 07 MLT (denoted by the red circle) with a value of 725 (MeV cm^2 sr s)$^{-1}$, a factor of ~1.8 lower than the mean intensity over all MLT. There is also a statistically significant peak in the microburst intensity at 2130 MLT (red circle) with a value of 1,660 (MeV cm^2 sr s)$^{-1}$, a factor of ~1.3 higher than the mean intensity over all MLT. The remainder of the

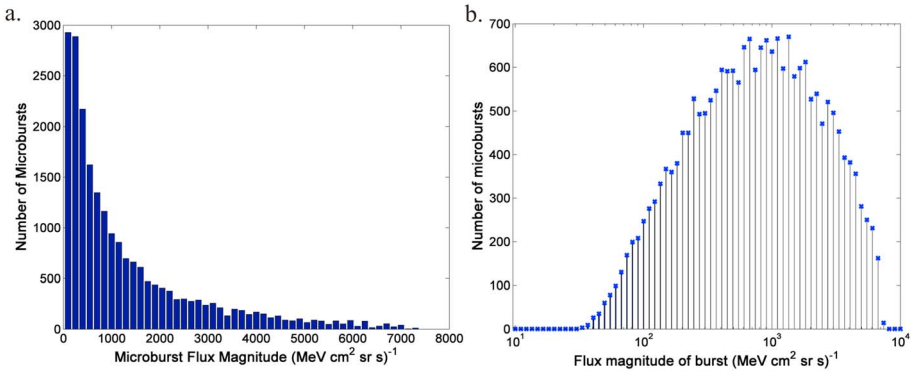

Figure 2. The distribution of relativistic microburst >1.05-MeV intensities on a (a) linear and (b) $\log_{10}$ scale.

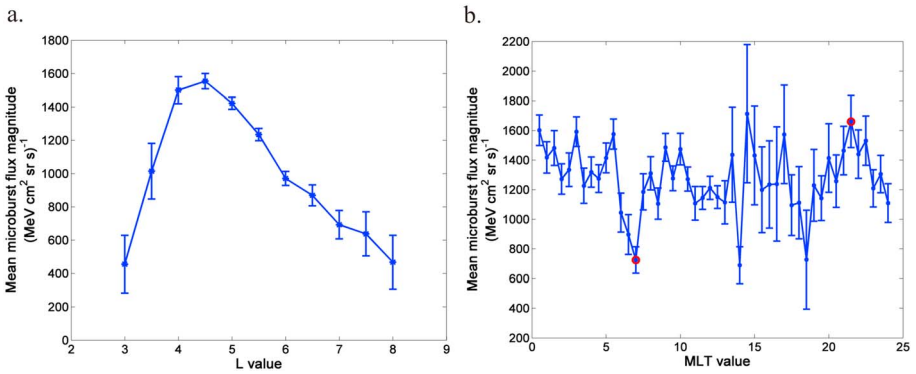

Figure 3. The (a) *L* and (b) MLT distributions of the mean relativistic microburst intensity and associated 95% confidence interval on the mean intensity. The red circles identify the statistically significant MLT variation. MLT = magnetic local time.

variation observed in Figure 3b is not statistically significant. The larger errors (95% confidence intervals) in the afternoon MLT region (from 13–19 MLT) are due to the smaller number of microbursts occurring in this MLT region.

In Figure 4 we present the combined *L* and MLT distribution of relativistic microburst median intensity at 0.5 *L* and 1-hr MLT resolution. As for the mean intensity, the median intensity is only calculated for *L* and MLT bins where ≥5 microbursts occur to ensure the averages are statistically representative. Figure 4 shows that the median intensity of relativistic microbursts increases (on average) with decreasing *L* shells. This effect is most pronounced at 10 MLT but can also be clearly observed at 00, 01, 05, 11, and 22 MLT. The median microburst intensity is low for the entire *L* range at 6 MLT and high for the entire *L* range at 21, 23, and 00 MLT. On average the median microburst intensities are higher in the 19–01 MLT range (following a counter clockwise rotation) and lower in the 03–12 MLT range.

Whistler mode chorus waves, which are thought to be the dominant driver of relativistic microbursts, have larger amplitudes in the morning MLT region (Li et al., 2009; Meredith et al., 2012). Thus, Figure 4 appears to suggest that the regions of highly active chorus waves drive (on average) lower-intensity microbursts. However, upon closer inspection of the relativistic microburst intensity distributions in a range of MLT

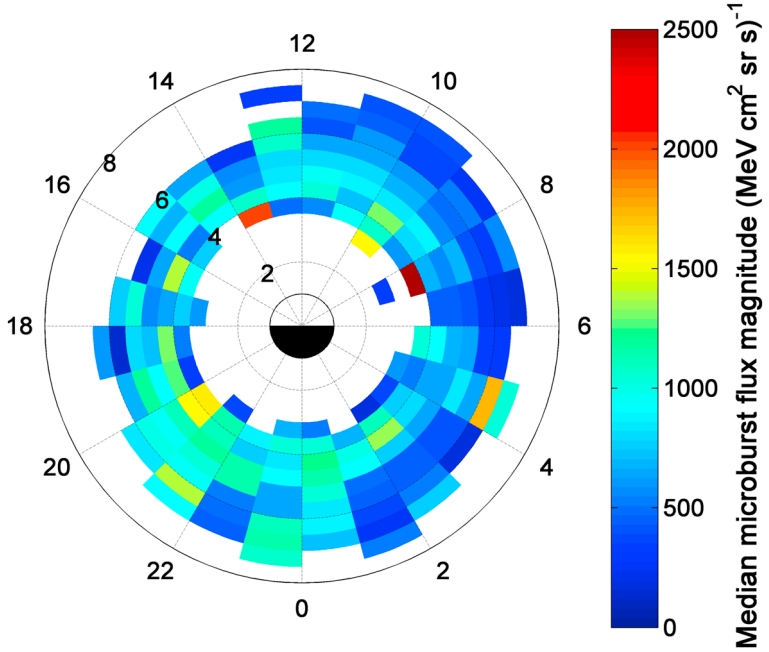

Figure 4. The *L* and magnetic local time distribution of the median relativistic microburst intensity.

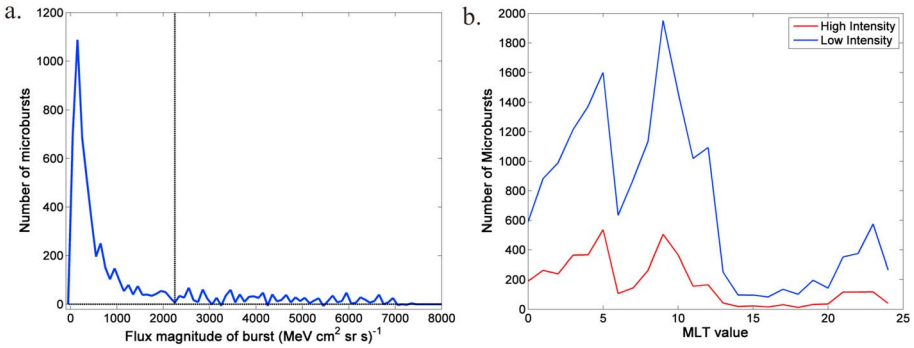

Figure 5. (a) The difference between relativistic microburst intensity distributions in the 03–11 MLT region and the 19–03 MLT region. (b) The MLT distribution of the number of microbursts detected with intensities above (red) and below (blue) 2,250 (MeV cm^2 sr s)$^{-1}$. MLT = magnetic local time.

regions (similar to those presented in Figure 2) we find this is not the case. Figure 5a presents the difference between the microburst intensity distributions in the 03–11 and the 19–03 MLT regions (again following a counterclockwise rotation). To clarify, in making Figure 5a we have found the distribution of microbursts with varying intensity in the 03–11 MLT range and subtracted it from the distribution of microbursts with varying intensity in the 19–03 MLT range. We also classify microbursts as being low or high intensity relative to a threshold value of 2,250 (MeV cm^2 sr s)$^{-1}$. This threshold is shown by the vertical black line in the figure. From Figure 5a it is clear that high-intensity relativistic microbursts (i.e., those >2,250 [MeV cm^2 sr s]$^{-1}$ have similar occurrences in the two MLT regions, as the difference between the number of bursts occurring in this range is very low. On the other hand, low-intensity microbursts (<2,250 [MeV cm^2 sr s]$^{-1}$) occur more often in the 03–11 MLT region when compared with the 19–03 MLT region.

This is also demonstrated in Figure 5b, which shows the number of relativistic microbursts occurring over MLT for the two different intensity ranges (high (red) and low (blue) intensities). From Figure 5b it is clear that the number of microbursts occurring in the 11–19 MLT region is low, and therefore, this region will not be discussed further. There is significantly less variation over MLT in the number of microbursts with intensities greater than 2,250 (MeV cm^2 sr s)$^{-1}$ (red line) than the number of microbursts with intensities below 2,250 (MeV cm^2 sr s)$^{-1}$ (blue line). Both the high- and low-intensity microbursts show a drop in activity around 06–07 MLT, consistent with the drop in the microburst intensity observed in this MLT region.

Thus, we find that in the 03–11 MLT region, which is where larger whistler mode chorus wave amplitudes are known to be present, there is a much higher number of comparatively low-intensity microbursts. This larger number of low-intensity microbursts results in the lower average intensity shown in Figure 4 for this MLT region. We suggest that the highly active chorus region is driving a greater number of low-intensity (intensities <2,250 [MeV cm^2 sr s]$^{-1}$) relativistic microbursts.

4.2. Plasmapause Location

We have also calculated how the mean intensity and duration of relativistic microbursts changes with various L distances from the plasmapause. We used the O'Brien and Moldwin (2003) *AE* model to find the location of the plasmapause at the times of the relativistic microbursts. In Figure 6a we present the mean microburst intensity, and in Figure 6b the mean microburst duration and their associated 95% confidence intervals for microbursts occurring in 0.25 L bands from the plasmapause. The red lines in Figures 6a and 6b indicate the location of the plasmapause, negative L bands correspond to inside the plasmasphere, while positive L bands correspond to the outside the plasmasphere. The black dashed lines in Figures 6a and 6b identify the mean microburst intensity over all the L bands.

As we move outward from the plasmapause in Figure 6a we observe the largest mean intensity for the relativistic microbursts occurs at 1.25 L from the plasmapause with a mean intensity of 1,484 (MeV cm^2 sr s)$^{-1}$. This L band is ~1 L closer to the plasmapause than the L band with the most frequent microburst activity (Douma et al., 2017). Moving inward from the plasmapause we note that the microburst intensity appears to increase. However, the low number of microbursts occurring inside the plasmasphere (Douma et al., 2017) results in the large confidence intervals observed in this region.

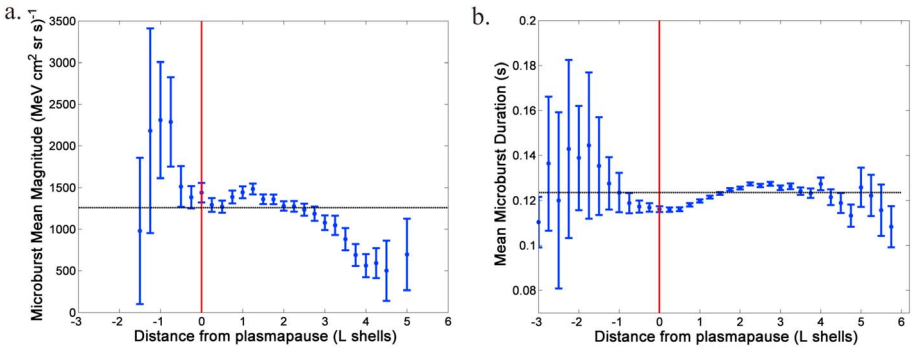

Figure 6. (a) The mean relativistic microburst intensity and (b) the mean relativistic microburst duration and their associated 95% confidence intervals at various distances from the plasmapause (red line). The black dashed line identifies the mean intensity/duration over all distances from the plasmapause.

As whistler mode chorus waves generally occur outside the plasmapause, one possible conclusion that might be drawn from Figure 6a is that the microbursts occurring outside the plasmapause are driven by whistler mode chorus waves, while those microbursts occurring inside the plasmapause are driven by EMIC waves. If this were the case we would expect different timescales of microburst precipitation inside and outside the plasmapause due to the very different plasma wave drivers. However, Figure 6b shows there is no statistically significant difference between the timescales of precipitation occurring inside and outside the plasmapause. This lack of any statistically significant differences is likely due to the low number of microbursts occurring inside the plasmapause. As such, it does not rule out EMIC waves as a potential driver of relativistic microbursts occurring inside the plasmasphere. However, the evidence presented here is not strong evidence in support of EMIC waves driving relativistic microbursts. Stronger evidence of this link was provided in Douma et al. (2018) who presented case study evidence of relativistic microbursts that may have been driven by EMIC waves.

4.3. Changes With Geomagnetic Activity

We now investigate how the mean intensity of relativistic microbursts changes under different levels of geomagnetic activity. In order to remain consistent with earlier work (e.g., Li et al., 2009; Douma et al., 2017), we have defined three levels of geomagnetic activity based on AE^* (the mean of AE over the previous 1 hr); quiet corresponds to $AE^* \leq 100$ nT, disturbed corresponds to $100 < AE^* \leq 300$ nT, and active corresponds to $AE^* > 300$ nT. However, our large relativistic microburst data set allows us to also extend these well used AE^* ranges to include higher geomagnetic activity; intense conditions correspond to $AE^* > 550$ nT and extreme conditions correspond to $AE^* > 750$ nT.

In Figure 7a we present the mean microburst intensity and associated 95% confidence interval over the five AE^* ranges. In Figure 7b we present the number of relativistic microbursts occurring over each AE^* range. Note the y axis in Figure 7a begins at 700 (MeV cm^2 sr s)$^{-1}$ to magnify the confidence intervals. There is no statistically significant difference between the mean microburst intensity during quiet and disturbed AE^* conditions, identified by the overlapping confidence intervals. The large confidence interval around the mean intensity of quiet AE^* microbursts is the result of the very small number of microbursts occurring in this AE^* range. However, there is a statistically significant increase in the mean microburst intensity from disturbed to extreme AE^* conditions, where there are greater numbers of microbursts occurring. The lowest mean intensity (occurring during disturbed AE^* conditions) is a factor of 1.7 lower than the highest mean intensity (occurring during extreme AE^* conditions). Thus, Figure 7a indicates that the mean relativistic microburst intensity increases as the level of geomagnetic activity increases, but only by a factor of about 1.7.

To further investigate the changes in microburst intensity over geomagnetic activity, we consider the L and MLT distributions of median microburst intensity over these AE^* ranges: quiet, disturbed, active, intense, and extreme AE^*. These distributions are presented in Figure 8. In this figure we again use 0.5 L and 1 MLT resolution and discuss all MLT ranges using a counterclockwise rotation. Note that this figure is on a linear scale. Quiet AE^* conditions (Figure 8a) do not contain enough microburst events to draw any conclusions about the L and MLT distribution of the median microburst intensity. From Figures 8b–8e it is clear that the

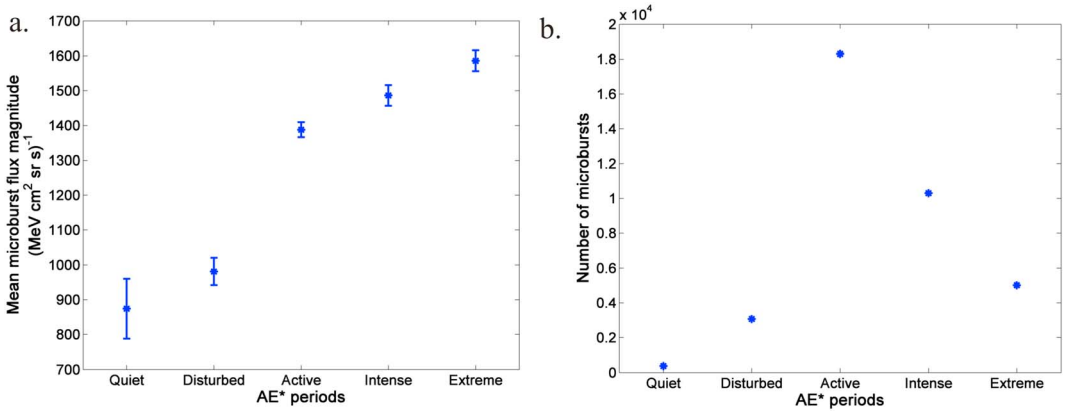

Figure 7. (a) The mean relativistic microburst intensity and associated 95% confidence interval for the mean intensity over five different *AE** ranges; quiet $AE^* \leq 100$ nT, disturbed $100 < AE^* \leq 300$ nT, active $AE^* > 300$ nT, intense $AE^* > 550$ nT, and extreme $AE^* > 750$ nT. (b) The number of relativistic microbursts occurring over the same five *AE** ranges.

overall median microburst intensity increases as the level of geomagnetic activity increases, although the level of variation is quite small.

From Figure 8 it also appears that the highest median microburst intensity occurs in the premidnight MLT region for disturbed *AE** conditions (Figure 8b) and moves toward the morning sector as the level of geomagnetic activity increases. The highest median microburst intensity occurs in the 08–10 MLT region during extreme *AE** conditions (Figure 8e). We investigate this trend further (not shown) using the microburst intensity distributions in the 03–11 and 19–03 MLT regions, as before. In the 03–11 MLT region the proportion of low-intensity (<2,250 [MeV cm^2 sr s]$^{-1}$) microbursts decreases with increasing geomagnetic activity while the proportion of high-intensity (>2,250 [MeV cm^2 sr s]$^{-1}$) microbursts increases. More specifically,

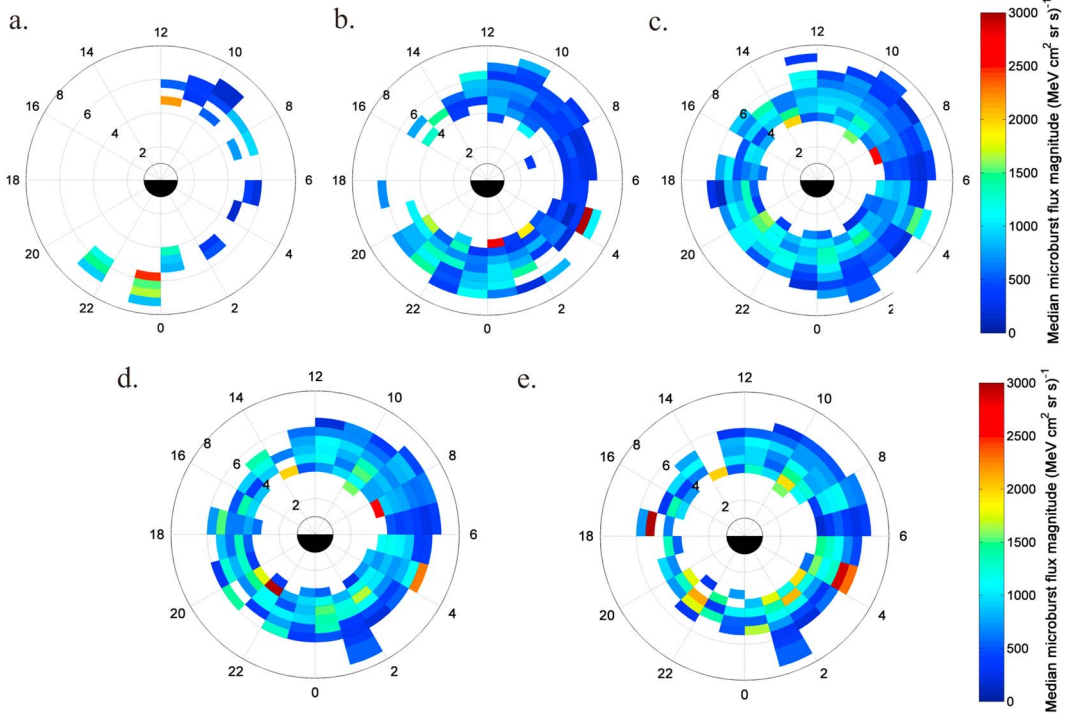

Figure 8. The *L* and magnetic local time distributions of the median relativistic microburst intensity during (a) quiet $AE^* \leq 100$ nT, (b) disturbed $100 < AE^* \leq 300$ nT, (c) active $AE^* > 300$ nT, (d) intense $AE^* > 550$ nT, and (e) extreme *AE** conditions $AE^* > 750$ nT.

the proportion of high-intensity microbursts in the 03–11 MLT region increases from ~20% to ~65% with increasing geomagnetic activity. In contrast, in the 19–03 MLT region the proportions of low-intensity and high-intensity microbursts remain relatively constant over the various geomagnetic conditions. More specifically, in the 19–03 MLT region 70–80% of the microbursts have low intensity and 20–30% have high intensity. These results suggest that the movement of the highest median microburst intensity toward morning MLT as geomagnetic activity levels increase is in fact evidence of a reducing proportion of low-intensity microbursts driven in the 03–11 MLT region.

These changing distributions of relativistic microburst intensities with varying levels of geomagnetic activity are suggestive of a change in the distribution of chorus wave power (thought to be the main driver of these precipitation events) with changing geomagnetic conditions.

5. Comparison to Observed Trapped Fluxes

We have accounted for the effect of the HILT saturation in the above microburst intensity analysis; however, we now need to consider the effect of variations in the trapped electron flux. One possibility is that the microburst intensity is limited by the magnitude or dynamics of the trapped flux present when the scattering process is occurring. In this study we use the HEO3 satellite to quantify the magnitude and temporal variation of trapped flux present near the geomagnetic equator (where the whistler mode chorus waves are generated and thought to interact with the relativistic electrons) at the time of the relativistic microbursts.

We use the high-altitude orbits of HEO3 as for these orbits the satellite spends significantly more time at $L > 4$. The even orbits (and odd orbits) sample the same pitch angle ranges but different ranges of MLT values. At energies >1 MeV we expect this MLT difference not to be significant, as the drift time is short. Comparing the HEO3 >1.5-MeV fluxes to the GOES10 >2-MeV trapped fluxes around $L = 6.6$, we find the best agreement between the two satellite trapped flux measurements occurs with the Even High Altitude Orbits (EHAOs) of HEO3 and as such these orbits will be used for the remainder of this analysis.

We compare the daily median >1.5-MeV trapped flux measured by HEO3 EHAO from $4.4 < L < 4.8$ to the daily median intensity of relativistic microbursts from $4.4 < L < 4.8$ for the year 2003, as presented in Figure 9a. The daily median microburst intensity is calculated for days where ≥5 microbursts are occurring to ensure the data set is statistically representative of the true microburst intensity. Our first glance at Figure 9a demonstrates that the daily median trapped flux varies by several orders of magnitude throughout 2003. In contrast, the daily median microburst intensity varies by less than an order of magnitude throughout 2003. Note that we have investigated the trapped fluxes and microburst intensities over the years 1999–2006 and a range of L intervals (not shown) finding very similar patterns to those presented in Figure 9a.

To aid the viewing of Figure 9a, we have selected a representative subset of daily median microburst intensities and categorized the magnitude and dynamics of the trapped flux associated with them by color-coded vertical lines. The yellow lines identify periods of trapped flux recoveries (back to the average values) after a dropout. The black lines identify periods of trapped flux recoveries (back to the average values) after an enhancement in the trapped fluxes. The cyan lines identify periods of increasing trapped flux values (above the average values). Lastly, the red lines identify dropouts of the trapped fluxes. We have selected a range of median daily relativistic microburst intensities; high (>6,500 [MeV cm^2 sr s]$^{-1}$), midrange (2,500–4,500 [MeV cm^2 sr s]$^{-1}$), and low (<1,000 [MeV cm^2 sr s]$^{-1}$).

The two periods with the highest daily median intensity microbursts (>6,500 [MeV cm^2 sr s]$^{-1}$) in Figure 9a occur in January and November of 2003. The January high-intensity microburst is associated with a recovery of the daily median trapped flux back to the average trapped flux, after a dropout occurred a few days previously (yellow). The November high-intensity microburst is associated with a recovery of the daily median trapped flux back to the average trapped flux, after an increase in the trapped flux occurred in the previous days (black).

The midrange subset of relativistic microburst intensities (2,500–4,500 [MeV cm^2 sr s]$^{-1}$) of Figure 9a occur in August, September, and November. The August and November midrange microburst intensities are associated with increases in the daily median trapped flux (cyan). The two September midrange microburst intensities are associated with recoveries of the daily median trapped flux following increases in the daily median trapped fluxes (black).

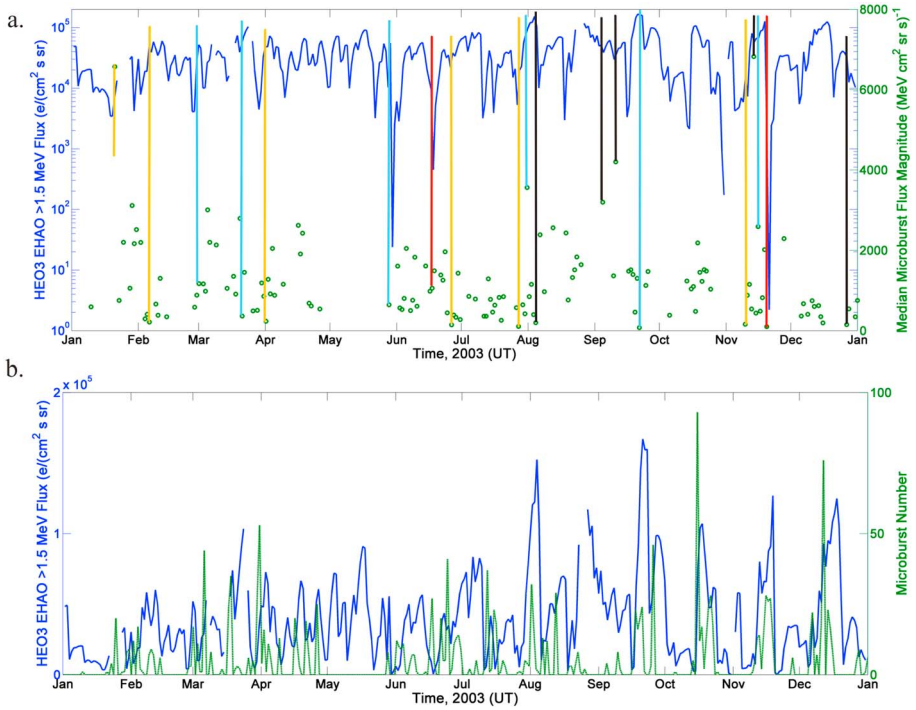

Figure 9. The HEO3 Even High Altitude Orbit (EHAO) daily median >1.5-MeV electron flux (blue) and (a) the median microburst intensity (green) with colored lines description given in the text and (b) the daily total number of microbursts occurring (green). All measurements are taken in 2003 around $L = 4.6$.

The low subset of relativistic microburst intensities (<1,000 [MeV cm^2 sr s]$^{-1}$) of Figure 9a occur in February, March, April, May, June, July, August, September, November, and December. The March, May, and September low-intensity microbursts are associated with increases in the daily median trapped fluxes (cyan). The August and December low-intensity microbursts are associated with recoveries of the daily median trapped fluxes following increases (black). The February, April, June, and July low-intensity microbursts are associated with recoveries of the daily trapped fluxes following dropouts (yellow). One of the November low-intensity microbursts is also associated with a recovery of the daily trapped flux following a dropout (yellow). The other November low-intensity microburst is associated with a dropout in the daily median trapped flux (red).

In Figure 9a we also identify a dropout in the daily median trapped fluxes occurring in June (red) associated with neither a high nor a low daily median microburst intensity.

If the relativistic microburst intensities were limited by the magnitude of trapped fluxes present at the time of the scattering process, we would expect to observe low median intensity microbursts associated with trapped flux dropouts and high median intensity microbursts associated with increases in trapped fluxes. However, during periods of low trapped fluxes (daily median <500 e/[cm^2 s sr]) we do not solely observe low-intensity microbursts and during periods of high trapped fluxes (daily median >80,000 e/[cm^2 s sr]) we do not solely observe high-intensity microbursts. Thus, we suggest that the microburst intensities are not limited by the magnitude (and similarly the variation) of trapped flux present at the time of the microburst scattering mechanism.

For completeness we also investigate whether the occurrence of relativistic microbursts is limited by the magnitude or dynamics of the trapped fluxes present at the time of the scattering process. Figure 9b presents the daily median >1.5-MeV trapped electron fluxes measured by HEO3 EHAO from $4.4 < L < 4.8$ (blue) and the daily total number of detected relativistic microbursts from $4.4 < L < 4.8$ (green) for 2003. The lack of relativistic microburst observations in May is due to a SAMPEX data outage.

In Figure 9b we observe increases in the number of detected microbursts associated with increases in the >1.5-MeV trapped electron fluxes. This is particularly evident in early March, early April, early August, late

September, mid-October, and mid-December. These increases in the number of detected microbursts appear to be associated with the leading edge of the trapped flux increases. The majority of days with trapped fluxes <8,000 e/(cm^2 s sr) have very little observed microburst activity (most evident in the latter half of 2003). In contrast, days with >70,000 e/(cm^2 s sr) trapped fluxes have greater numbers of relativistic microbursts, ranging from 20–100 microbursts detected daily.

We have investigated this relationship between the trapped fluxes and microburst activity over the years 1999–2006 and a range of L intervals (not shown) and find similar patterns to those presented in Figure 9b. Thus, we suggest the number of relativistic microbursts observed is related more closely to the dynamics of the trapped flux, with more microbursts occurring when the trapped population is enhancing. We further suggest that the occurrence of relativistic microbursts may be linked to the processes causing the increasing trapped fluxes. This would be consistent with the concept that whistler mode chorus waves both scatter some electrons to produce microbursts and also accelerate some electrons, leading to increases in the trapped relativistic fluxes. Kurita et al. (2016) also observed this phenomenon during their case study storm in October 2012.

6. Conclusions

In this study we have addressed the lack of knowledge about the relativistic microburst intensity. We have used the O'Brien et al. (2003) algorithm to identify relativistic microbursts in the SSD4 channel of the SAMPEX HILT instrument. We have also applied the Blum et al. (2015) extension to the detection algorithm to obtain the intensity of the detected relativistic microbursts. Our analysis of the relativistic microburst intensity is limited to the North Atlantic Region, where a total of 21,746 relativistic microbursts was observed to occur.

The majority of the detected microbursts have intensities between 100 and 1,000 (MeV cm^2 sr s)$^{-1}$. The average microburst intensity peaks at $L = 4.5$ and 1.25 L beyond the plasmaspause. Considering the combined L and MLT distributions of relativistic microburst intensity, we find the intensity increases as we move inward in L. Additionally, the number of high-intensity microbursts (>2,250 [MeV cm^2 sr s]$^{-1}$) remains roughly constant over all MLT regions, while the number of low-intensity microbursts (<2,250 [MeV cm^2 sr s]$^{-1}$) is significantly higher in the 03–11 MLT region.

The mean microburst intensity increases by a factor of 1.7 as the geomagnetic activity level increases (as measured by the AE* index). Additionally, the proportion of high-intensity relativistic microbursts (>2,250 [MeV cm^2 sr s]$^{-1}$) in the 03–11 MLT region increases from ~20% to ~65% as geomagnetic activity increases. In contrast, the proportion of high-intensity relativistic microbursts in the 19–03 MLT region remains constant at ~20–30% as geomagnetic activity increases. We suggest that these changing distributions of relativistic microburst intensities with geomagnetic activity are the result of a change in the whistler mode chorus wave activity, which are thought to be the main driver of these precipitation events.

We have used the EHAO of the HEO3 satellite to estimate the quantity of trapped electrons (with energies >1.5 MeV) at the time of the relativistic microbursts. A comparison to these trapped fluxes suggests that the relativistic microburst intensities are not limited by the level of trapped flux present at the time of the scattering processes. However, the number of relativistic microbursts occurring does appear to correspond to the level of trapped flux, with more relativistic microbursts occurring when the trapped fluxes are enhancing, suggesting that the microbursts are linked to the processes causing the increased trapped fluxes. This is consistent with whistler mode chorus waves scattering some electrons (resulting in relativistic microbursts) and accelerating some electrons (resulting in the enhanced trapped fluxes).

In the following appendix we have used the AE9 model to estimate the impact of relativistic microbursts on a flux tube. We find a large difference between the loss timescales of the statistically average microburst rate and spectra and the extreme microburst rate and spectra. However, given our finding potentially linking microbursts to periods of electron acceleration, it is difficult to draw direct conclusions around loss timescales when both processes are occurring.

Appendix A: Comparison to Modeled Trapped Fluxes

Previous studies (e.g., Breneman et al., 2017; Lorentzen et al., 2001; Millan et al., 2002) have investigated the impact relativistic microbursts have on the electron populations contained within the radiation belts.

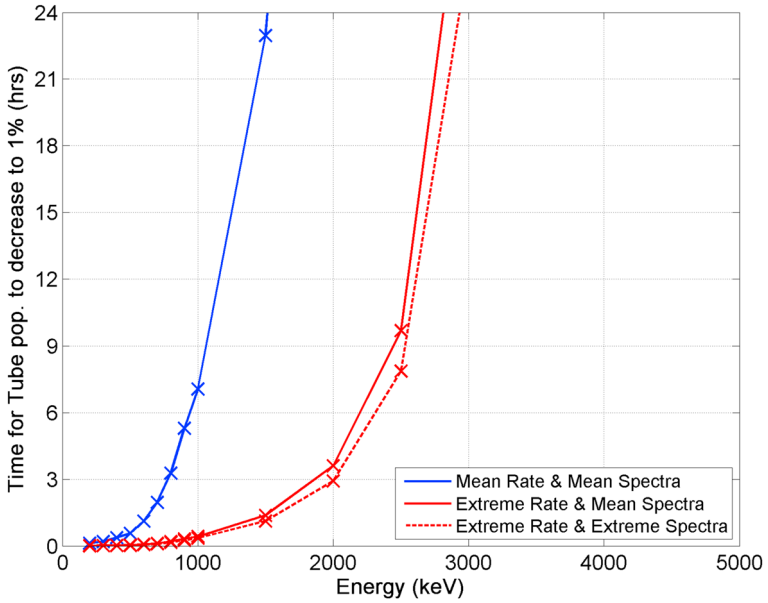

Figure A1. The timescale of a reduction to 1% in the flux tube at a given energy due to a statistically average relativistic microburst rate and intensity (blue), an extreme rate and statistically average intensity (red solid), and an extreme microburst rate and intensity (red dashed).

However, most of these studies use a rough estimate of the total electron content in the radiation belts. In contrast, the recent study by Breneman et al. (2017) estimates the total number of electrons present in a flux tube using the Van Allen Probes data.

In this study we use the AE9 model (IRENE; Johnston et al., 2017) to estimate the total number of electrons present in a flux tube with 1-cm^2 area at 100-km altitude and $L = 4.43$ following the approach outlined in Rodger et al. (2003). With the AE9 modeled trapped flux levels in a given flux tube we will be able to perform a first order simplistic calculation of the time taken for microbursts to empty the flux tube. We apply the statistically average microburst spectra presented in Seppälä et al. (2018), which is in close agreement with the spectra published in Crew et al. (2016). These spectra are based on modeling work presented in Rodger et al. (2007) and are valid from 100 keV to to 7 MeV. Using these spectra, we calculate how many microbursts it would take to reduce the flux tube population of any given energy (in the range 100 keV to 7 MeV) to 1%. We then apply the statistically average microburst occurrence rate of three microbursts per minute (discussed in greater detail in Seppälä et al., 2018) and the extreme microburst occurrence rate of 50 microbursts per minute (based on an extreme case that will be discussed in a future study) to estimate the time taken to reduce the total flux tube population at any given energy down to 1%.

While we have made attempts to account for the sporadic occurrence and varying scale size of microbursts (by applying statistically average microburst spectra and rate), our calculation will only give us a first-order, simplistic estimate of the microburst loss timescales. In reality, the microburst loss will occur across a range of MLT values (corresponding to the MLT range of active whistler mode chorus wave activity) on a given drift shell, rather than being limited to a flux tube. As such the timescales of electron loss from the radiation belts due to microbursts are likely to be longer than those we have calculated.

Presented in Figure A1 is the estimate of the microburst loss timescales, where the blue line corresponds to the statistically average microburst rate and spectra, the solid red line corresponds to the extreme microburst rate and the statistically average spectra, and the dashed red line corresponds to the extreme microburst rate and spectra. Note we have increased the magnitude of the statistically average microburst spectra to produce the extreme microburst spectra, which reflects the higher-intensity microbursts occurring during the extreme case study period.

From Figure A1 we observe that trapped electrons with energies below ~500 keV are removed from the flux tube within 1 hr under all microburst rates and spectra. Using the statistically average microburst rate and spectra, we note that trapped electrons with 1-MeV energies are removed from the flux tube on

timescales of ~7 hr, while 2-MeV electrons are lost from the flux tube on timescales of ~23 hr. Using the extreme microburst rate and statistically average intensity, we note that the losses from the flux tube occur much faster. Under these conditions the 1-MeV electrons are lost within 1 hr and the 2-MeV electrons are lost within 4 hr. The loss of the relativistic electrons (>1 MeV) is noticeably faster when using the extreme microburst rate and spectra, with 2-MeV electrons being lost within 3 hr. These conditions correspond to the fastest timescales of loss we expect from microburst activity. Overall, Figure A1 shows that microburst activity rate has a large impact on the loss timescales of electrons from a given flux tube in the radiation belts. It further shows that the microburst spectra have a significant impact on the loss timescales of relativistic (>1 MeV) from a given flux tube. We suggest that additional information on the spectra (and energy range) of relativistic microbursts is required before conclusive studies can be made about the impact relativistic microbursts (and lower-energy microbursts) have on the trapped fluxes in the radiation belts.

An additional caveat of this study is that the AE9 model does not account for any acceleration processes that may be increasing the trapped population inside a flux tube. As we showed earlier it appears as though the microbursts are occurring alongside increases in the trapped fluxes (Figure 9b), which likely result from the acceleration of lower-energy electrons to megaelectron volt energies. This acceleration may be replenishing the megaelectron volt electron content of the radiation belts and thus adding to the total flux tube population. This would mask the microburst precipitation signal in the trapped fluxes and make it difficult to use experimental trapped flux data to determine the exact timescale and extent of the relativistic microburst electron loss from the radiation belts and their subsequent impact on the atmosphere.

Acknowledgments
E. Douma was supported by a University of Otago publishing bursary. Data availability is described at the following websites: http://www.srl.caltech.edu/sampex/DataCenter/Index.html (SAMPEX), wdc.kugi.kyoto-u.ac.jp (*AE*), and virbo.org/HEO (HEO3).

References

Agapitov, O., Blum, L. W., Mozer, F. S., Bonnell, J. W., & Wygant, J. (2017). Chorus whistler wave source scales as determined from multipoint Van Allen Probe measurements. *Geophysical Research Letters*, *44*, 2634–2642. https://doi.org/10.1002/2017GL072701

Agapitov, O., Mourenas, D., Artemyev, A., Mozer, F. S., Bonnell, J. W., Angelopoulos, V., et al. (2018). Spatial extent and temporal correlation of chorus and hiss: Statistical results from multipoint THEMIS observations. *Journal of Geophysical Research: Space Physics*, *123*, 8317–8330. https://doi.org/10.1029/2018JA025725

Anderson, B. R., Shekhar, S., Millan, R. M., Crew, A. B., Spence, H. E., Klumpar, D. M., et al. (2017). Spatial scale and duration of one microburst region on 13 August 2015. *Journal of Geophysical Research: Space Physics*, *122*, 5949–5964. https://doi.org/10.1002/2016JA023752

Baker, D. N., Mason, G. M., Figueroa, O., Colon, G., Watzin, J. G., & Aleman, R. M. (1993). An overview of the Solar, Anomalous, and Magnetospheric Particle Explorer (SAMPEX) mission. *IEEE Transactions on Geoscience and Remote Sensing*, *31*, 531–541. https://doi.org/10.1109/36.225519

Blake, J. B., Baker, D. N., Turner, N., Ogilvie, K. W., & Lepping, R. P. (1997). Correlation of changes in the outer-zone relativistic-electron population with upstream solar wind and magnetic field measurements. *Geophysical Research Letters*, *24*, 927–929. https://doi.org/10.1029/97GL00859

Blum, L. W, Li, X., & Denton, M. (2015). Rapid MeV electron precipitation as observed by SAMPEX/hilt during high-speed stream-driven storms. *Journal of Geophysical Research: Space Physics*, *120*, 3783–3794. https://doi.org/10.1002/2014JA020633

Breneman, A. W., Crew, A., Sample, J., Klumpar, D., Johnson, A., Agapitov, O., et al. (2017). Observations directly linking relativistic electron microbursts to whistler mode chorus: Van Allen Probes and FIREBIRD II. *Geophysical Research Letters*, *44*, 11,265–11,272. https://doi.org/10.1002/2017GL075001

Crew, A. B., Spence, H. E., Blake, J. B., Klumpar, D. M., Larsen, B. A., O'Brien, T. P., et al. (2016). First multipoint in situ observations of electron microbursts: Initial results from the NSF FIREBIRD II mission. *Journal of Geophysical Research: Space Physics*, *121*, 5272–5283. https://doi.org/10.1002/2016JA022485

Dietrich, S., Rodger, C. J., Clilverd, M. A., Bortnik, J., & Raita, T. (2010). Relativistic microburst storm characteristics: Combined satellite and ground-based observations. *Journal of Geophysical Research*, *115*, A12240. https://doi.org/10.1029/2010JA015777

Douma, E., Rodger, C. J., Blum, L. W., & Clilverd, M. A. (2017). Occurrence characteristics of relativistic electron microbursts from SAMPEX observations. *Journal of Geophysical Research: Space Physics*, *122*, 8096–8107. https://doi.org/10.1002/2017JA024067

Douma, E., Rodger, C. J., Clilverd, M. A., Hendry, A. T., Engebretson, M. J., & Lessard, M. R. (2018). Comparison of relativistic microburst activity seen by SAMPEX with ground-based wave measurements at Halley, Antarctica. *Journal of Geophysical Research: Space Physics*, *123*, 1279–1294. https://doi.org/10.1002/2017JA024754

Greeley, A. D., Kanekal, S. G., Baker, D. N., Klecker, B., & Schiller, Q. (2019). Quantifying the contribution of microbursts to global electron loss in the radiation belts. *Journal of Geophysical Research: Space Physics*. https://doi.org/10.1029/2018JA026368

Johnston, W. R., O'Brien, T. P., Ginet, G., Huston, S., Guild, T., Roth, C., et al. (2017). Irene: AE9/AP9/SPM radiation environment model. *Users Guide*, *version 1.20.001*.

Klecker, B., Hovestadt, D., Scholer, M., Arbinger, H., Ertl, M., H, Kastle, et al. (1993). Hilt: A heavy ion large area proportional counter telescope for solar and anomalous cosmic rays. *IEEE Transactions of Geoscience and Remote Sensing*, *31*, 542–548. https://doi.org/10.1109/36.225520

Kurita, S., Miyoshi, Y., Blake, J. B., Reeves, G. D., & Kletzing, C. A. (2016). Relativistic electron microbursts and variations in trapped MeV electron fluxes during the 8–9 october 2012 storm: SAMPEX and Van Allen Probes observations. *Geophysical Research Letters*, *43*, 3017–3025. https://doi.org/10.1002/2016GL068260

Li, W., Thorne, R. M., Angelopoulos, V., Bortnik, J., Cully, C. M., Ni, B., et al. (2009). Global distribution of whistler-mode chorus waves observed on the THEMIS spacecraft. *Geophysical Research Letters*, *36*, L09104. https://doi.org/10.1029/2009GL037595

Lorentzen, K. R., Looper, M. D., & Blake, J. B. (2001). Relativistic electron microbursts during GEM storms. *Geophysical Research Letters*, *28*, 2573–2576. https://doi.org/10.1029/2001GL012926

Meredith, N. P., Horne, R. B., Sicard-Piet, A., Boscher, D., Yearby, K. H., Li, W., & Thorne, R. M. (2012). Global model of lower band and upper band chorus from multiple satellite observations. *Journal of Geophysical Research*, *117*, A10225. https://doi.org/10.1029/2012JA017978

Millan, R. M., Lin, R. P., Smith, D. M., Lorentzen, K. R., & McCarthy, M. P. (2002). X-ray observations of MeV electron precipitation with balloon-borne germanium spectrometer. *Geophysical Research Letters*, *29*(24), 2194. https://doi.org/10.1029/2002GL015922

Nakamura, R., Baker, D. N., Blake, J. B., Kanekal, S., Klecker, B., & Hovestadt, D. (1995). Relativistic electron precipitation enhancements near the outer edge of the radiation belt. *Geophysical Research Letters*, *22*, 1129–1132. https://doi.org/10.1029/95GL00378

O'Brien, T. P., Fennell, J. F., Roeder, J. L., & Reeves, G. D. (2007). Extreme electron fluxes in the outer zone. *Space Weather*, *5*, S01001. https://doi.org/10.1029/2006SW000240

O'Brien, T. P., Lorentzen, K. R., Mann, I. R., Meredith, N. P., Blake, J. B., Fennell, J. F., et al. (2003). Energization of relativistic electrons in the presence of ulf wave power and MeV microbursts: Evidence for dual ULF and VLF acceleration. *Journal of Geophysical Research*, *108*, SMP11. https://doi.org/10.1029/2002JA00978

O'Brien, T. P., & Moldwin, M. B. (2003). Empirical plasmapause models from magnetic indices. *Geophysical Research Letters*, *30*(4), 1152. https://doi.org/10.1029/2002GL016007

Omura, Y., Nunn, D., Matsumoto, H., & Rycroft, M. J. (1991). A review of observational, theoretical and numerical studies of VLF triggered emissions. *Journal of Atmospheric and Solar Terrestrial Physics*, *53*, 351–368.

Omura, Y., & Zhao, Q. (2013). Relativistic electron microbursts due to nonlinear pitch angle scattering by EMIC triggered emissions. *Journal of Geophysical Research: Space Physics*, *118*, 5008–5020. https://doi.org/10.1002/jgra.50477

Reeves, G., McAdams, K. L., Friedel, R. H. W., & O'Brien, T. P. (2003). Acceleration and loss of relativistic electrons during geomagnetic storms. *Geophysical Research Letters*, *30*(10), 1529. https://doi.org/10.1029/2002GL016513

Ripoll, J.-F., Chen, Y., Fennell, J. F., & Friedel, R. H. W. (2015). On long decays of electrons in the vicinity of the slot region observed by HEO3. *Journal of Geophysical Research: Space Physics*, *120*, 460–478. https://doi.org/10.1002/2014JA020449

Rodger, C. J., Clilverd, M. A., & McCormick, R. J. (2003). Significance of lightning-generated whistlers to inner radiation belt electron lifetimes. *Journal of Geophysical Research*, *108*, 1462. https://doi.org/10.1029/2003JA009906

Rodger, C. J., Clilverd, M. A., Nunn, D., Verronen, P. T., Bortnik, J., & Turunen, E. (2007). Storm time, short-lived bursts of relativistic electron precipitation detected by subionospheric radio wave propagation. *Journal of Geophysical Research*, *112*, A07301. https://doi.org/10.1029/2007JA012347

Santolik, O., Macusova, E., Titova, E. E., Kozelov, B. V., Gurnett, D. A., Pickett, J. S., et al. (2008). Frequencies of wave packets of whistler-mode chorus inside its source region: A case study. *Annales Geophysicae*, *26*, 1665–1670.

Sazhin, S. S., & Hayakawa, M. (1992). Magnetospheric chorus emissions: A review. *Planetary Space Science*, *40*, 681–697.

Seppälä, A, Douma, E., Rodger, C. J., Verronen, P. T., Clilverd, M. A., & Bortnik, J. (2018). Relativistic electron microburst events: Modeling the atmospheric impact. *Geophysical Research Letters*, *45*, 1141–1147. https://doi.org/10.1002/2017GL075949

Shumko, M., Sample, J., Johnson, A., Blake, B., Crew, A., Spence, H., et al. (2018). Microburst scale size derived from multiple bounces of a microburst simultaneously observed with the FIREBIRD-II Cube-Sats. *Geophysical Research Letters*, *45*, 8811–8818. https://doi.org/10.1029/2018GL078925